Relaxation of angular momentum in fission and quasifission reactions

B. B. Back
Argonne National Laboratory, Argonne, Illinois 60439

S. Bjørnholm and T. Døssing
Niels Bohr Institute, DK-2100 Copenhagen, Denmark

W. Q. Shen,* K. D. Hildenbrand, and A. Gobbi
Gesellschaft für Schwerionenforschung, D-6100 Darmstadt, Federal Republic of Germany

S. P. Sørensen
University of Tennessee, Knoxville, Tennessee 37996
(Received 9 November 1989)

Binary reaction products from reactions of a ^{238}U beam at energies 5.4, 5.9, 6.7, and 7.5 MeV/nucleon with targets of ^{16}O, ^{26}Mg, ^{27}Al, ^{32}S, ^{35}Cl, ^{40}Ca, ^{48}Ca, and ^{nat}Zn have been measured with a kinematic coincidence method. The γ-ray multiplicities are measured at the same time with NaI detectors and presented as a function of fragment mass. The results indicate that all aligned and statistically excited spin modes of the fragments are fully populated in compound nucleus fission reactions. In quasifission reactions the relaxation processes seem to terminate before full statistical spin equilibrium is reached. The results are analyzed and discussed in terms of various dinuclear spin modes with different characteristic relaxation times. The influence of various terminal freeze-out shapes is also discussed.

I. INTRODUCTION

Dissipation is a very conspicuous feature of heavy-ion reactions. The dissipative force opposing the relative motion has both a radial and a tangential component, and so it is not surprising to find a strong tendency towards transfer of relative angular momentum into aligned rotation of the two reaction partners in binary heavy-ion reactions.[1-4] Along with this transfer of oriented angular momentum from relative to internal rotation, the reaction partners also acquire angular momentum through diffusion.[5] Subject to the constraint of conservation of total angular momentum, diffusion tends towards a statistical equilibrium, i.e., a situation where each rotational degree of freedom of the two reaction partners acquires a mean rotational energy equal to $\frac{1}{2}T$, where T is the temperature.[6] Thus, even in central collisions, the reaction products will emerge with nonzero angular momentum. The smaller the reaction angular momentum and the higher the temperature, the more the diffusive, statistical angular momentum components will dominate the total angular momenta and hence the γ-ray multiplicities of the final products.

Recently, the one-body window dissipation model was applied to study the angular momentum dynamics in deep-inelastic reactions. The angular momentum distribution was found to approach the statistical equilibrium distribution, but with widely different time scales for the different statistical models.[7] Since window friction implies a strong inhibition of the relaxation of the mass asymmetry mode, this detailed description cannot be applied to the quasifission reactions, whose very characteristic is the substantial mass drift during a short reaction time. The mass relaxation rate in quasifission reactions can actually be explained by the wall friction mechanism,[8,9,11] but so far the angular momentum dynamics has not been described theoretically for the more compact shapes, which are relevant for quasifission.

There are, on the other hand, measurements of the relaxation of one of the statistical spin modes in quasifission reactions, namely the tilting mode, or K mode; see Fig. 1. This mode can be studied separately by measuring angular distributions, because it is the only mode that affects the orientation of the dinuclear system with respect to the total spin. Thus, in a detailed study of the reaction between ^{208}Pb and ^{40}Ar, ^{50}Ti, or ^{58}Fe, Lützenkirchen *et al.*[12] find that the tilting mode is quite far from reaching an equilibrium value appropriate to the saddle shape within the available reaction time of $5-10\times10^{-21}$ s. It does not even reach the (smaller) value expected at scission.

In the more slowly evolving compound fission reactions there is ample experimental evidence that the K mode can reach equilibrium appropriate to the saddle.[13-16] Since the K mode is expected to have the longest relaxation time according to theory,[7,17] one expects in effect all modes to be fully equilibrated in compound fission reactions. This is also what is found by Schmitt *et al.* in their study based on γ-ray multiplicity measurements in compound nucleus fission reactions.[18] The observed γ-ray multiplicity and hence spin distributions are quite flat when plotted as a function of the fragment mass asymmetry.[18,19] This is understood as the result of a

weak, u-shaped contribution from the aligned spins with a minimum at symmetry, superimposed with a slightly n-shaped contribution from the statistical spin modes.

Similarly, flat γ-multiplicity distributions are found for compound fission reactions in a previous study[20] of Pb-induced reactions with the target ^{26}Mg. In contrast to the flat distributions, pronounced n-shaped distributions were found in the same experiment in reactions with heavier targets, where quasifission dominates. The closer the fragment masses are to the initial masses, the smaller the multiplicity. There is both qualitative and quantitative evidence that mass drift and reaction time are closely correlated in quasifission reactions.[8,9,21] The n-shaped multiplicity distributions are therefore suggestive of an incomplete, time-dependent relaxation of important spin modes.

Relaxation of aligned and statistical spin modes is the subject of this paper. It is based on previously published results,[20] and on new γ-multiplicity measurements with a uranium beam of energies varying from 5.4 to 7.5 MeV/nucleon. The targets range from ^{16}O to ^{nat}Zn, and thus both compound fission, but in particular quasifission reactions, are studied. The observed energy, mass, and angular distributions from these reactions have already been published.[8,9] A particularly striking result (obtained from the angle versus mass distribution) is the finding that the mass drift towards symmetry can be described as an exponential relaxation process. It was found that a "universal" relaxation time of 5×10^{-21} s, independent of beam energy (i.e., temperature) as well as target mass gives a good description of the data.[8,9] During the total reaction time, defined as the time elapsed from the moment the in-going nuclei leave their Coulomb trajectories to the final fragment join theirs, there appears in addition to be a period of a duration of about 10^{-21} s, where no mass drift occurs.[9] Presently, we exploit these results by simply viewing the observed final fragment masses as indicators of the reaction time.

In this work we have studied the multiplicity of the γ-ray cascades emitted in the dexcitation of the final fragments in order to obtain a measure of the average spins carried by the fragments. The multiplicity is recorded as a function of their mass and excitation energy. Relevant parameters for the systems studied are listed in Table I. One main result emerging from this work is the observed dominance of spin modes acquired through diffusion, over the aligned spin components, generated by tangential friction. From the analysis of the data it becomes clear, however, that the observed γ multiplicities cannot be explained by a simple statistical model in which thermal equilibrium is assumed at a well-specified stage of the evolution of the dinuclear system. Rather, it appears that the dinuclear spin modes are gradually being excited with characteristic times that are often longer than the reaction time, and substantially longer than expected on the basis of the window dissipation model, valid for deep-inelastic reactions. Since the trajectories leading to the quasifission reactions are thought to proceed through rather compact mononuclear shapes, it is puzzling that the relaxation towards equilibrium of the various spin modes proceeds on such a slow time scale. This is contrary to what one observes, when comparing mass asymmetry relaxation in deep-inelastic and quasifission reactions.

The paper is organized as follows. Section II describes the experiments with the uranium beam. Section III presents the new results on γ multiplicities, together with a recapitulation of previous results[20] obtained with a lead beam. Section IV outlines the statistical equilibrium model, and compares its predictions to the measured results. Especially the question of the compactness of the reaction complex as well as that of the angular momen-

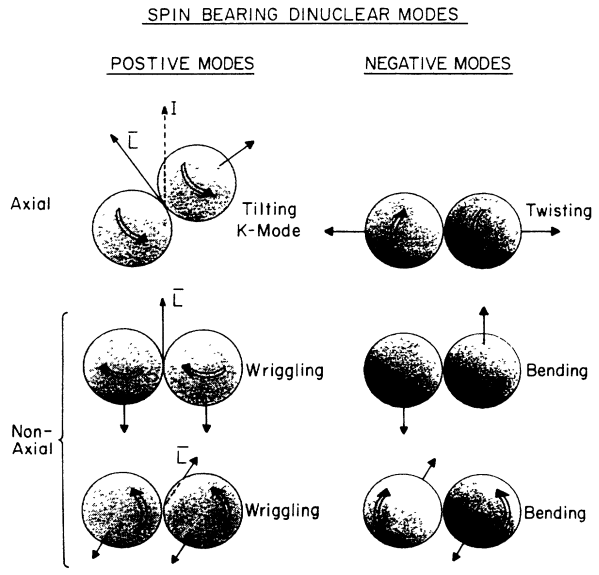

FIG. 1. Schematic illustration of the six statistical spin modes of a dinuclear system based on Ref. 6.

TABLE I. Properties of the systems produced in the reactions with ^{238}U beams. The third through fifth columns give the following quantities: third—the fission barrier for $l=0$ obtained from the finite range liquid-drop model of Sierk (Ref. 22); fourth—the angular momentum for which the fission barrier vanishes (Ref. 22); and fifth—the total kinetic energy for symmetric fission obtained from the relation $E_K=1.24Z^2_{CN}/A^{1/3}_{CN}$ (MeV), which corresponds to distance between fragment centers of $d=1.83$ fm.

Target	Composite system	$B_f(l=0)$ (MeV)	$l_{B_f=0}$ ($\hbar$)	E_K^{calc} (MeV)
^{16}O	^{254}Fm	1.80	64	196
^{26}Mg	$^{264}_{104}X$	0.86	56	209
^{27}Al	$^{265}_{105}X$	0.76	52	212
^{32}S	$^{270}_{108}X$	0.31	42	223
^{35}Cl	$^{273}_{109}X$	0.23	39	227
^{40}Ca	$^{278}_{112}X$	0.12	27	238
^{48}Ca	$^{286}_{112}X$	0.13	32	236
^{nat}Zn	$^{302}_{122}X$			275

tum fractionation are thoroughly discussed. Finally, a summary and conclusion of the findings is presented in Sec. V.

II. EXPERIMENTAL ARRANGEMENT

In this experiment we have measured the γ-ray multiplicity associated with fission and quasifission fragments of ^{238}U-induced reactions. The two fissionlike products were measured in four large-area (20×30 cm^2) x-y position-sensitive avalanche detectors, placed in the foward hemisphere and operated in kinematic coincidence. A schematic view of the experimental arrangement is shown in Fig. 2. By measuring the position and time of the product, as it penetrates the detector, the velocity vector of the particle can be determined by taking advantage of the pulsed nature of the ^{238}U beam obtained from the GSI Unilac accelerator. The binary nature of the reaction was verified event by event and the primary (preneutron emission) kinematics calculated, leading to a determination of masses, center-of-mass scattering angle, and total kinetic energy. This procedure is described in more detail in Ref. 9.

The beam energies used in this experiment were $E_{\rm lab}=5.4$, 5.9, 6.7, and 7.5 MeV/nucleon and the beam intensities were typically $\sim$0.1 particle nA. Targets of ^{26}Mg, ^{27}Al, Li ^{35}Cl, ^{40}Ca ^{16}O, ^{48}Ca ^{16}O, and $^{\rm nat}$Zn ^{32}S of thickness in the range 100–300 μg/cm^2 were used. The Mg, LiCl, and ZnS targets were deposited on carbon backings of about 20 μg/cm^2 thickness. In the case of the Ca target, we took advantage of the rapid oxidation of the originally pure metallic Ca foils.

Reactions on the individual target constituents were separated event by event on the basis of the kinematic requirements for two-body final states, i.e., the fragments must be emitted colinearly within a narrow cone, in a center-of-mass frame of reference appropriate to each particular target constituent.

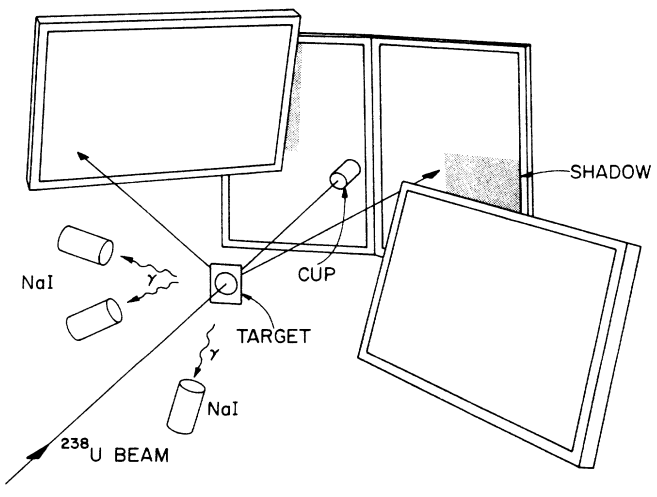

FIG. 2. Schematic illustration of the experimental arrangement used in this work.

Coincident γ rays were measured in three 7.5×7.5 cm diam. NaI were detectors placed at backward angles at a distance of 15 cm from the target. These detectors were centered at angles of $\theta,\phi=(90°,0°)$, (90°,45°), and (175°,22.5°), respectively. Thin sheets of Cu and Pb absorber material were placed in front of the NaI detectors in order to suppress the abundant low-energy x rays emanating from the target. This also has the effect of producing an approximately constant efficiency curve at the low γ-ray energies.

The total efficiency of the NaI detectors was measured by placing γ-ray sources of ^{137}Cs and ^{60}Co of known strength at the target position. By counting for a known length of time, the efficiency of the detectors can be determined from the source strength and the total number of counts in the γ-ray spectrum. It was found that the efficiency was constant to within $\pm5\%$ over the $\sim$200–1500 keV range of γ-ray energies. The efficiencies determined in this fashion were checked by placing a ^{252}Cf source at the target position and detecting, in coincidence, the fission fragments and the associated γ rays in the avalanche detectors and the NaI detectors, respectively. The resulting γ-ray multiplicities were found to coincide, within 10%, with the results of Gerschel *et al.*[10]

Examples of the observed γ-ray spectra are shown in Fig. 3. We observe that the bulk of the γ intensity lies within the 200–1500 keV constant region of the NaI efficiency curve. The fact that the efficiency starts to fall off for energies above 1500 keV is therefore inconsequential for the γ-ray multiplicity measurements.

Since the inverse kinematics employed in the present experiment gives rise to substantial velocities (3–4 cm/ns) of the fragments in the laboratory frame of reference, corrections for the difference in solid angle of the NaI detectors are required. Average Jacobian correction factors, which fall in the range ($f_{\rm Jacoby}=1.2$–1.35), have been applied to the measured γ multiplicity.

The large forward velocity of the quasifission fragments does, however, effectively suppress another possible source of background in the data, namely the numerous neutrons emitted from the hot fragments after scission. In order to be counted as a prompt coincidence a neutron must generate a signal in a NaI detector within ±5 ns of the point in time when the beam pulse strikes the target. This requires a velocity of 3–4 cm/ns to compensate for the forward directed velocity of the fragments plus a velocity of 3 cm/ns in order to travel the 15 cm distance from the target to the NaI detector within the 5 ns time window allowed for "prompt" coincidence events. The neutron must therefore be emitted with a velocity of 6–7 cm/ns in the center-of-mass frame of reference of the emitting fragment in order to be mistaken for a prompt γ ray. Since this neutron velocity corresponds to an energy of more than 20 MeV, we estimate that the background associated with neutrons is extremely small. This estimate is based on the low probability of emission of neutrons with energies above this threshold from fragments with temperatures of less than about 3 MeV, as is

the case in this experiment. An example of the time spectrum of the NaI-detector events measured with respect to the beam pulse is shown in Fig. 4.

On the basis of the discussion of the various experimental uncertainties and corrections presented above we estimate that the overall systematic accuracy of the measured γ-ray multiplicity may be as large as 10–15 percent. The error bars shown on subsequent figures of the data represent only the statistical counting uncertainty, which is the relevant quantity, when assessing the systematic trends seen in the data.

III. EXPERIMENTAL RESULTS

A. Overall results of γ-multiplicity measurements

The γ multiplicities obtained from the present experiment are listed in Table II, and shown as solid points as a function of fragment mass for the different beam energies and targets in Figs. 5 and 6. The fragment mass is the one recorded in the avalanche detectors positioned on the right-hand side of the beam, the complementary fragment being detected in the counters on the left-hand side of the

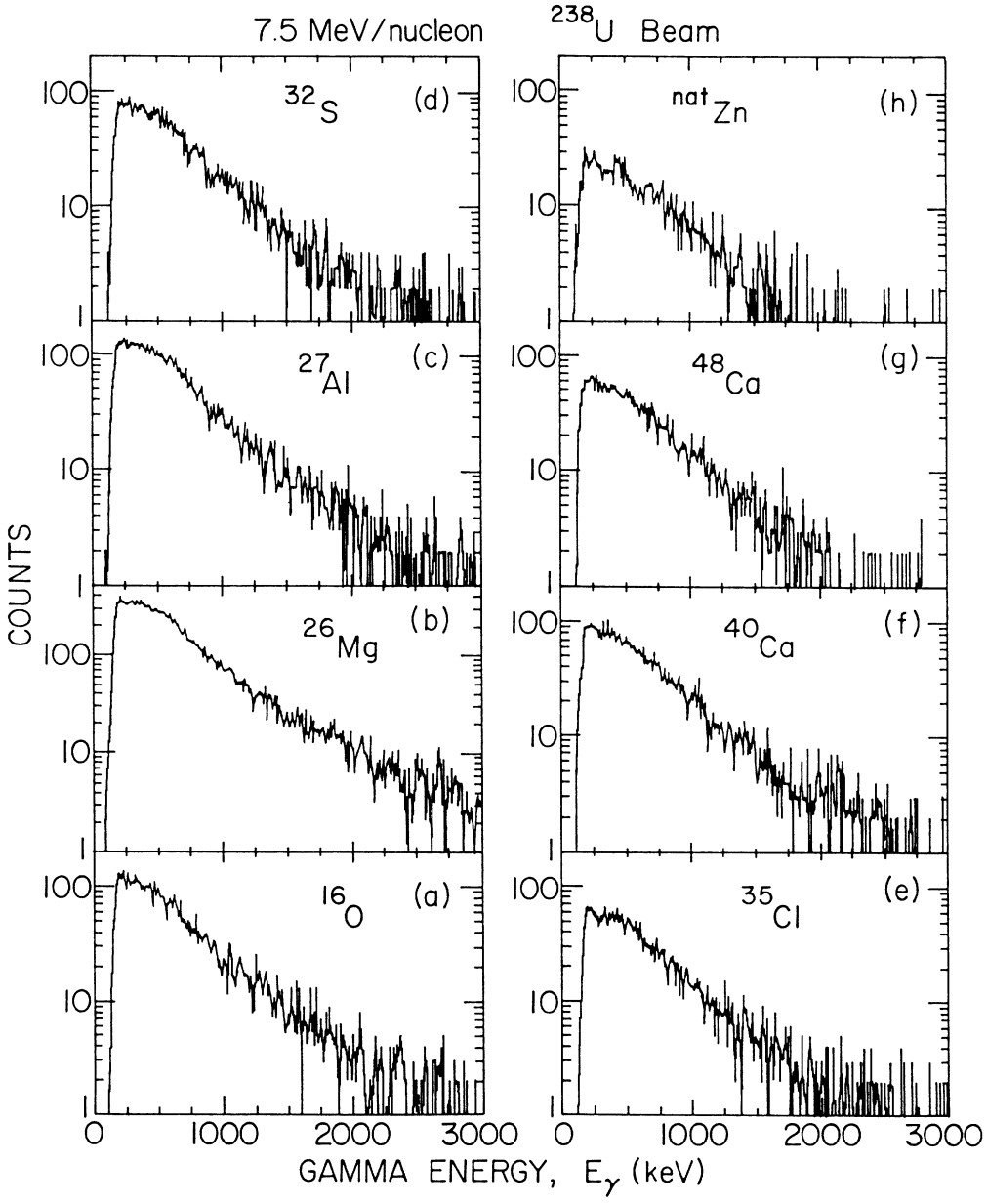

FIG. 3. Gamma-ray spectra measured in coincidence with quasifission fragments are shown for 7.5 MeV/nucleon ^{238}U beam on the targets indicated in the figure. The low-energy cutoff at about 150 keV is caused by a fast discriminator.

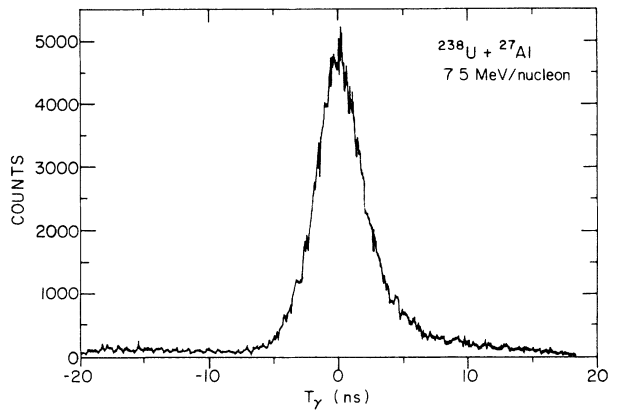

FIG. 4. Time spectrum of events in the NaI detectors measured with respect to the time structure of the beam.

beam. Any asymmetry in the data between complementary mass fragments must therefore be ascribed to geometrical asymmetries of the setup or to minor experimental inaccuracies in the determination of the relevant physical parameters (angles, velocities, and masses of the fragments). Such asymmetries in the data are seen to be weak, less than 5% in almost all cases. It shows that there are no systematic errors present that may obscure the global trends in the γ-ray multiplicity measured as a function of mass division for the various scattering systems.

Some trends in the experimental data are immediately obvious and worth noticing. Whereas the γ-ray multiplicity is virtually independent of the fragment mass for some of the lighter targets e.g., ^{16}O and ^{26}Mg, we observe an increasing tendency to maxima in the γ multiplicity

TABLE II. Experimental results from this experiment. The second through seventh columns give the following quantities: second—the beam energy, $(E/A)_{\rm lab}$ (MeV/nucleon); third—the excitation of the compound system E^* (MeV); fourth—the nuclear temperature of the compound system given as $T_{\rm CN}=\sqrt{E^*\times 8.5/A_{\rm CN}}$ (MeV); fifth—the critical angular momentum for capture reactions (complete fusion and quasifission) $l_{\rm capture}$ ($\hbar$); sixth—the parameter $T_{\rm CN}^{1/2}A_{\rm CN}^{5/6}$; and seventh—the measured γ multiplicity $M_\gamma^{\rm sym}$ for symmetric mass division.

Reaction	$(E/A)_{\rm lab}$ (MeV)	$E^*_{\rm CN}$ (MeV)	$T_{\rm CN}$ ($\hbar$)	$l_{\rm capture}$	$T_{\rm CN}^{1/2}A_{\rm CN}^{5/6}$	$M_\gamma^{\rm sym}$
^{238}U+^{16}O	5.4	42.7	1.19	10	110.1	14.7±0.4
	5.9	50.2	1.30	27	115.1	15.5±0.4
	6.7	62.2	1.44	41	121.1	16.4±0.7
	7.5	74.1	1.58	48	126.9	17.1±0.7
^{238}U+^{26}Mg	5.4	52.5	1.30	30	118.8	17.2±0.4
	5.9	64.2	1.44	51	125.1	18.1±0.4
	7.5	101.7	1.81	93	140.2	19.6±0.4
^{238}U+^{27}Al	5.4	51.3	1.28	27	118.3	18.3±0.4
	5.9	63.4	1.43	42	125.0	19.0±0.4
	6.7	82.8	1.63	73	133.5	20.3±0.4
	7.5	102.4	1.81	86	140.6	21.7±0.4
^{238}U+^{32}S	5.4	47.8	1.23	13	117.8	14.1±1.7
	6.7	84.4	1.63	70	135.6	20.0±0.6
	7.5	107.0	1.84	89	144.1	23.7±0.6
^{238}U+^{35}Cl	5.4	48.7	1.23	24	118.9	17.3±0.8
	5.9	63.9	1.41	49	127.3	19.8±0.4
	6.7	88.3	1.66	82	138.1	19.6±0.5
	7.5	112.8	1.87	95	146.6	23.3±0.4
^{238}U+^{40}Ca	5.4	44.7	1.17	8	117.7	13.8±1.9
	5.9	61.8	1.37	32	127.4	15.3±0.4
	6.7	89.2	1.65	73	139.8	23.8±0.4
	7.5	116.6	1.89	95	149.6	26.7±0.4
^{238}U+^{48}Ca	5.4	52.7	1.25	73	124.6	19.7±0.4
	5.9	72.7	1.47	98	135.1	23.3±0.4
	6.7	104.6	1.76	119	147.8	25.1±0.4
	7.5	136.6	2.01	143	158.0	27.3±0.4
^{238}U+$^{\rm nat}$Zn	5.4	96.0	1.64	18	150.1	9.1±1.2
	6.7	180.5	2.25	88	175.9	25.2±0.4
	7.5	232.5	2.55	109	187.2	31.7±0.7

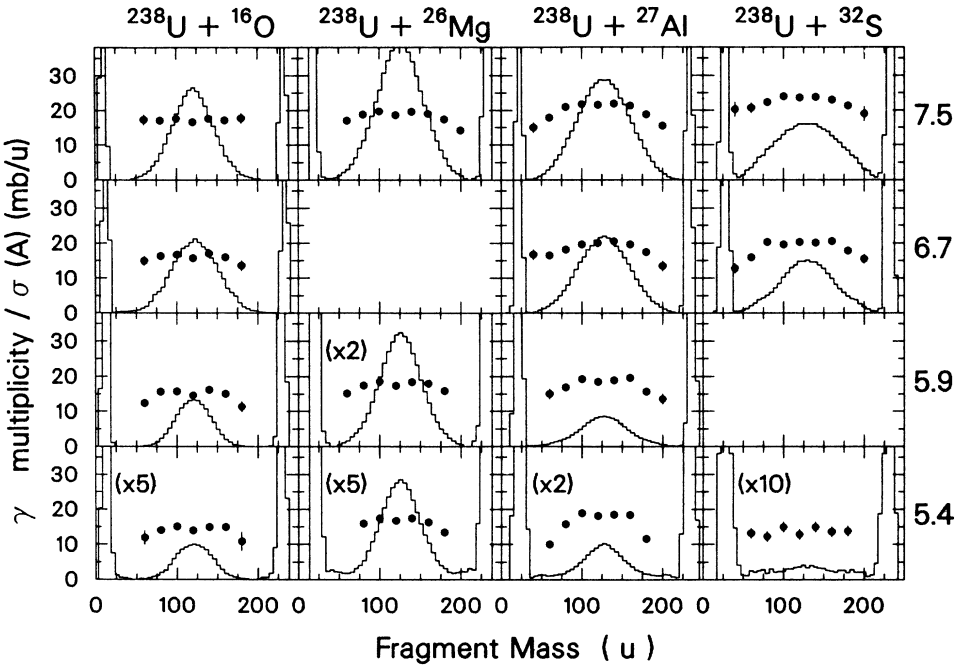

FIG. 5. Average γ-ray multiplicities shown as a function of the mass of one of the final products for the reactions $^{238}U+^{16}O$, ^{26}Mg, ^{27}Al, and ^{32}S at beam energies of 5.4, 5.9, 6.7, and 7.5 MeV/nucleon, solid circles. The measured mass yields, integrated over all angles, are shown as thin-line histograms.

for symmetric mass splits and lower values for more asymmetric mass splits in reactions on heavier targets. The reason for this trend will be studied in greater detail in the following section.

In addition, we see the expected trend that the γ-ray multiplicity increases with bombarding energy. Both the total angular momentum and the excitation energy of the system increase with the bombarding energy. The in-

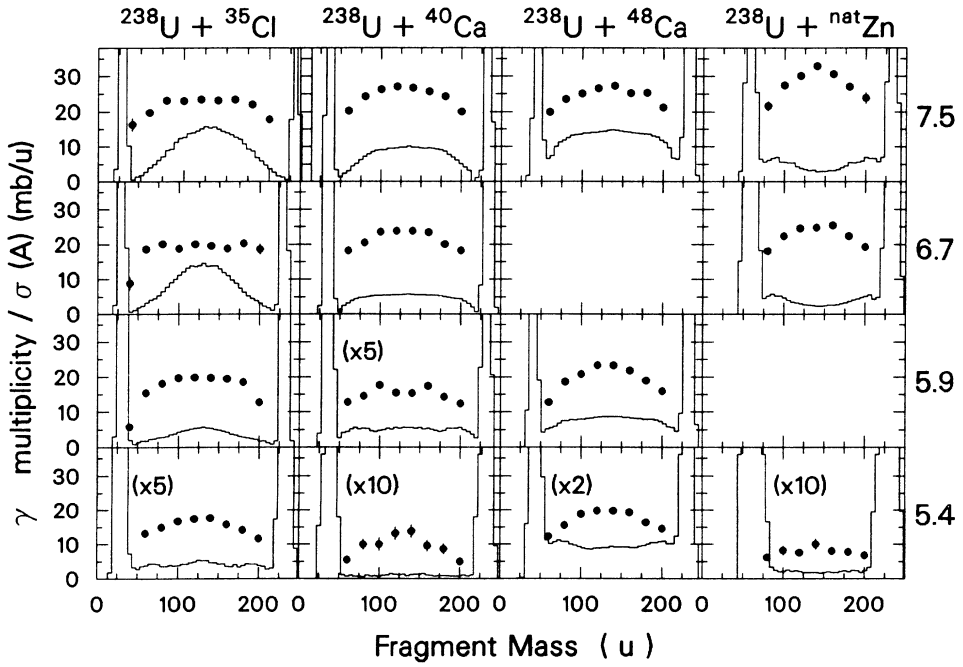

FIG. 6. Average γ-ray multiplicities shown as a function of the mass of one of the final products for the reactions $^{238}U+^{35}Cl$, ^{40}Ca, ^{48}Ca, and ^{nat}Zn at beam energies of 5.4, 5.9, 6.7, and 7.5 MeV/nucleon, solid circles. The mass distributions are also shown here.

creasing angular momentum implies an increase in the amount of aligned spin transferred to the nuclei due to tangential friction. At the same time the increasing excitation energy implies an increase in the spin fluctuations generated by diffusion. In early studies of γ-ray multiplicities in deeply inelastic scattering reactions,[2,23] the transfer of angular momentum from the relative target-projectile motion to individual fragment spins was emphasized. This is to some extent justified by the large l values associated with these reactions. The importance of the thermal excitations of fragment spin modes, as originally evidenced by the bending mode observed in spontaneous fission of ^{252}Cf,[24] has however been recognized; and it has been studied in both dynamical[5,25] and statistical[6] descriptions. In Sec. IV we will look closer at the relative importance of aligned and thermally generated spin, respectively, in producing the observed γ-ray multiplicities.

B. Systematics for symmetric mass split

In an attempt to assess already here the relative importance of the aligned and statistical parts of the spin excitations in the reaction products, we display the measured γ-ray multiplicities for symmetric mass splits as a function of three different parameters. First, versus the critical, i.e., upper, angular momentum for capture leading to quasifission reactions, we present Fig. 7(a). The solid points represent the data from this experiment, whereas the data from Ref. 20 are shown as open circles for comparison. The relatively large spread in the data indicates that the mechanism of spin transfer from the orbital motion is not the dominant mechanism for fragment spin excitations. In Fig. 7(b) the same data are shown as a function of the excitation energy of the fused system. In this case we see a somewhat stronger correlation. The uranium and lead data do, however, show a distinctly higher degree of correlation if plotted [Fig. 7(c)] as a function of the parameter $T_{\rm CN}^{1/2}A_{\rm CN}^{5/6}$. We can understand this strong correlation by assuming that a thermal equilibrium is established for the symmetric mass splits. We then expect that the excitation energy associated with each statistical spin mode is $\frac{1}{2}T$, where T is the nuclear temperature. Therefore

$$\frac{\langle S_i^2\rangle}{2\mathcal{I}_i}=\tfrac{1}{2}T\ , \tag{1}$$

where S_i and $\mathcal{I}_i$ are the spin and moment of inertia associated with the specific mode in question, respectively. Since the moment of inertia of any fixed shape scales with $A^{5/3}$, we find

$$\langle S_i^2\rangle \propto \mathcal{I}_i T \propto A_i^{5/3}T \tag{2}$$

or

$$\langle S_i\rangle \propto A_{\rm CN}^{5/6}T_{\rm CN}^{1/2}\ . \tag{3}$$

The observed correlation with this parameter therefore appears at first glance to prove that thermal excitation is the dominant source of fragment spins.

A closer look reveals a more complicated situation: It is normally assumed that the γ-ray multiplicity scales with the total fragment spin according to $M_\gamma = S/2+6$. This relation reflects the assumption that three statistical γ rays, carrying no spin on the average, are emitted from each fragment, and that the fragment spin is removed by the emission of stretched quadrupole transitions. For

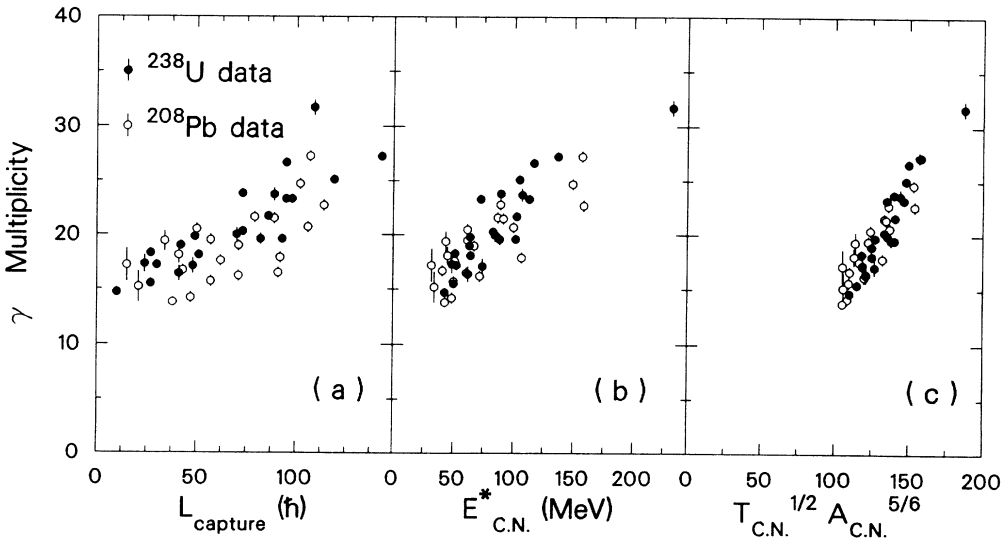

FIG. 7. The experimentally measured γ-ray multiplicities at mass symmetry of this work (solid circles) and the work by Bock *et al.* (Ref. 20) (open circles) are shown as a function of (i) the critical angular momentum for capture, $L_{\rm capture}$ [panel (a)], (ii) the excitation energy of the compound system, $E^*_{\rm CN}$ [panel (b)], and (iii) the parameter $T_{\rm CN}^{1/2}A_{\rm CN}^{5/6}$ [panel (c)].

thermal equilibrium at a given dinuclear freeze-out shape, this description predicts that the γ-ray multiplicities should lie on a straight line in Fig. 7(c) intersecting the ordinate at the multiplicity value +6. As seen from Fig. 7(c), the line suggested by the data does not agree with this expectation. It rather appears to have its intersection at a negative value of the multiplicity.

This rather dramatic contradiction compels us to reconsider the significance of the orbital angular momentum transfer to the fragments, and to look at different freeze-out shapes in more detail. In the following section we will therefore explore these aspects within a statistical equilibrium model making various assumptions about the angular momentum fractionation, and about the geometry of the dinuclear complex at the point at which the equilibrium spin excitation for symmetric mass splits is assumed to freeze out.

IV. THEORETICAL ANALYSIS OF THE RESULTS

A. The statistical spin distribution

Our basis for comparison with the data is the statistical equilibrium distribution of spins. This was first developed by Nix and Swiatecki[26] to describe the distribution of angular momentum is fission reactions, and then later extended and applied to damped nuclear reactions by Moretto, Schmitt, and Pacheco.[6,27] In its simplest form, the geometry of the interacting nuclei is taken as two touching spheres, as illustrated in Fig. 8.

The coordinate system adopted here for studying the spin distribution is defined by the axis connecting the centers of mass of the two parts of the reacting system (chosen as the z axis), and the projection of the total angular momentum onto the plane perpendicular to the z axis (chosen as the y axis). Note that this coordinate system (labeled $x'y'z'$ in Ref. 7) is the one originally proposed by Moretto.[6] This is convenient for small total angular momenta, or when one is only interested in spin magnitudes, and not in the directional distribution of the spins. for dynamical studies, and for studying the directional distributions, a coordinate system aligned with the orbital rotation (labeled xyz in Ref. 7) is preferable.

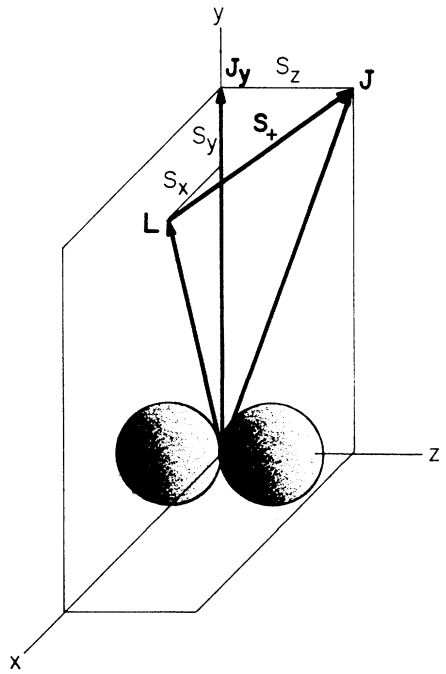

FIG. 8. Schematic illustration of the $\mathbf{J}_y$-aligned coordinate system used in this work.

The angular-momentum-dependent part of the macroscopic Hamiltonian may be written as

$$\mathcal{H}_{\rm rot}=\frac{1}{2\mathcal{I}_A}\mathbf{S}_A^2+\frac{1}{2\mathcal{I}_B}\mathbf{S}_B^2+\frac{1}{2\mathcal{I}_R}\mathbf{L}^2\ , \tag{4}$$

where $\mathbf{S}_A$ and $\mathbf{S}_B$ denote the spins of the two fragments, $\mathcal{I}_A$ and $\mathcal{I}_B$ are the associated moments of inertia, and $\mathcal{I}_R=\mu R^2$ denotes the orbital moment of inertia. The statistical modes describe excitation of the total and relative spins, respectively (defined in analogy to the total and relative momentum of the translational motion of two particles)

$$\mathbf{S}_+\equiv\mathbf{S}_A+\mathbf{S}_B,\quad \mathbf{S}_-\equiv\mathcal{I}_-\left[\frac{\mathbf{S}_A}{\mathcal{I}_A}-\frac{\mathbf{S}_B}{\mathcal{I}_B}\right]\ , \tag{5}$$

with moments of inertia

$$\mathcal{I}_+\equiv\mathcal{I}_A+\mathcal{I}_B,\quad \mathcal{I}_-=\frac{\mathcal{I}_A\mathcal{I}_B}{\mathcal{I}_A+\mathcal{I}_B}\ , \tag{6}$$

respectively. Using these spin variables, we may write

$$\mathcal{H}_{\rm rot}=\frac{1}{2\mathcal{I}_+}\mathbf{S}_+^2+\frac{1}{2\mathcal{I}_-}\mathbf{S}_-^2+\frac{1}{2\mathcal{I}_R}(\mathbf{J}-\mathbf{S}_+)^2\ . \tag{7}$$

In order to bring the rotational Hamiltonian [Eq. (7)] to normal form we follow Ref. 7 and introduce the auxilliary spin variable (in which the aligned y component of the fragment spins are removed)

$$\mathbf{s}=\mathbf{S}_+-\frac{\mathcal{I}_+}{\mathcal{I}_T}J_y\mathbf{y}\ , \tag{8}$$

where $\mathcal{I}_T=\mathcal{I}_++\mathcal{I}_R$ is the total rigid moment of inertia of the system perpendicular to the center axis, J_y is the y component of the total spin $\mathbf{J}$ (which has no x component), and $\mathbf{y}$ is a unit vector along the y axis (see Fig. 8).

Noting that $J_z=s_z$ and $J_x=0$ we find

$$\begin{aligned}\mathcal{H}_{\rm rot}&=\frac{1}{\mathcal{I}_+}s_x^2+\frac{1}{2\mathcal{I}_R}(0-s_x)^2+\frac{1}{2\mathcal{I}_+}\left[s_y+\frac{\mathcal{I}_+}{\mathcal{I}_T}J_y\right]^2\\&\quad+\frac{1}{2\mathcal{I}_R}\left[J_y-\frac{\mathcal{I}_+}{\mathcal{I}_T}J_y-s_y\right]^2+\frac{1}{2\mathcal{I}_+}s_z^2+\frac{1}{2\mathcal{I}_-}\mathbf{S}_-^2\\&=\frac{1}{2\mathcal{I}_T}\mathbf{J}^2+\frac{\mathcal{I}_T}{2\mathcal{I}_+\mathcal{I}_R}(s_x^2+s_y^2)\\&\quad+\frac{\mathcal{I}_R}{2\mathcal{I}_+\mathcal{I}_T}s_z^2+\frac{1}{2\mathcal{I}_-}\mathbf{S}_-^2\ ,\end{aligned} \tag{9}$$

where the first term corresponds to the yrast energy, the second term is the energy in the two orthogonal wriggling modes, the third term is the energy in the axial tilting mode, and the last term is the energy of the three negative modes.

Assuming that these modes are thermally excited, their population is governed by the Boltzmann factor $\exp(-\mathcal{H}_{\rm rot}/T)$, and each will have an excitation energy corresponding to half the nuclear temperature $\frac{1}{2}T$. We therefore find[27,7] for the *wriggling* modes,

$$(\sigma_+^2)_x=(\sigma_+^2)_y=\frac{\mathcal{I}_R}{\mathcal{I}_T}\mathcal{I}_+T\ ,$$

for the *tilting* mode,

$$(\sigma_+^2)_z=\frac{\mathcal{I}_T}{\mathcal{I}_R}\mathcal{I}_+T\ ,$$

for the *negative* modes,

$$(\sigma_-^2)_x=(\sigma_-^2)_y=(\sigma_-^2)_z=\mathcal{I}_-T\ , \tag{10}$$

where T is the nuclear temperature. The mean spins, directed along the y axis, are given by

$$\langle(S_+)_y\rangle=\left\langle\frac{\mathcal{I}_+}{\mathcal{I}_T}J_y+s_y\right\rangle=\frac{\mathcal{I}_+}{\mathcal{I}_T}\langle(J^2-J_z^2)^{1/2}\rangle$$
$$\simeq\frac{\mathcal{I}_+}{\mathcal{I}_T}\left[J-\frac{\langle s_z^2\rangle}{2J}\right]=\frac{\mathcal{I}_+}{\mathcal{I}_T}\left[J-\frac{(\sigma_+^2)_z}{2J}\right]\ , \tag{11}$$

whereas

$$\langle(S_+)_x\rangle=\langle(S_+)_z\rangle=\langle(S_-)_x\rangle=\langle(S_-)_y\rangle$$
$$=\langle(S_-)_z\rangle=0\ ,$$

where J is the total angular momentum, and it is assumed that $J^2\gg\sigma_+^2$. Here the first term of $\langle(S_+)_y\rangle$ describes a rigid rotation of the reaction complex, whereas the second term is a small correction connected with the choice of coordinate system.

The tilting variance is limited by the upper bound $J^2/3$, and for small J it will attain this value. We account for this in our calculations in a rather crude way, by keeping expressions (10) and (11), and then simply imposing the upper bound:

$$(\sigma_+^2)_z=\min\left[\frac{\mathcal{I}_T}{\mathcal{I}_R}\mathcal{I}_+T,\frac{J^2}{3}\right]\ . \tag{12}$$

The spin distributions in the two nuclei are derived from the mean spins (11) and variances (10) and (12) using the transformation (5). Neglecting terms of $(\sigma_+^2)_y/J$ and higher order we obtain the following expressions for the spin variances and the average spin of fragment A:

$$(\sigma_A^2)_x=\left[\frac{\mathcal{I}_A}{\mathcal{I}_T}\right]^2\langle S_+^2\rangle_x+\langle S_-^2\rangle_x$$
$$=\left[\frac{\mathcal{I}_A}{\mathcal{I}_T}\right]^2(\sigma_+^2)_x+(\sigma_-^2)_x$$
$$=\left[\frac{\mathcal{I}_R}{\mathcal{I}_T}\mathcal{I}_A^2+\mathcal{I}_A\mathcal{I}_B\right]\frac{T}{\mathcal{I}_+}\ , \tag{13}$$

$$(\sigma_A^2)_y\simeq\left[\frac{\mathcal{I}_R}{\mathcal{I}_T}\mathcal{I}_A^2+\mathcal{I}_A\mathcal{I}_B\right]\frac{T}{\mathcal{I}_+}\ , \tag{14}$$

$$(\sigma_A^2)_z=\left[\frac{\mathcal{I}_T}{\mathcal{I}_R}\mathcal{I}_A^2+\mathcal{I}_A\mathcal{I}_B\right]\frac{T}{\mathcal{I}_+}\ , \tag{15}$$

$$\langle(S_A)_y\rangle=\frac{\mathcal{I}_A}{\mathcal{I}_+}\langle(S_+)_y\rangle=\frac{\mathcal{I}_A}{\mathcal{I}_T}\left[J-\frac{(\sigma_+^2)_z}{2J}\right]\ ;$$
$$\langle(S_A)_x\rangle=0;\quad\langle(S_A)_z\rangle=0\ . \tag{16}$$

Analogous expressions apply to the average spin and spin variances for fragment B.

The sum of the fragment spins may be evaluated by numeric integration of the spin distribution function as defined by these moments.

Figure 1 illustrates the types of rotational motion described by the total and relative spins. For the positive modes, wriggling and tilting, the nuclei rotate in the same sense, and to conserve angular momentum, this motion is accompanied by some orbital rotation. This explains the factors containings $\mathcal{I}_R$ and $\mathcal{I}_T$ in the resulting variances of the spin of these modes. The negative modes, bending and twisting, describe opposite rotation of the two nuclei relative to each other, and do not involve any orbital rotation.

B. Statistical-model results for a heavy target nucleus

The statistical distribution can readily be found for shapes other than touching spheres. A rather extreme choice of geometry corresponds to the scission shape, as inferred from the Viola systematics for the kinetic energy of the final fragments[28,9] under the assumption of negligible prescission kinetic energy. This choice would be justified if all spin modes relax as fast as the radial momentum. (According to window friction, the two wriggling modes relax about a factor of 4 faster than the average value of the radial momentum, and the remaining four modes relax much slower.) The Viola systematics[28] implies a substantial elongation of the scission shape. The simplest realization of the Viola scission configuration consists of two spherical nuclei connected by a long neck of infinitesimal radius, the center distance between the nuclei being $1.83(A_1^{1/3}+A_2^{1/3})$ fm, A_1 and A_2 denoting the fragment mass numbers. The various spin modes (except maybe for the wriggling modes) are probably frozen in at a more compact shape, which for illustration we may take as two spheres at about touching distance, with a considerable neck connecting them.

The details of how to estimate the temperatures for the Viola shapes and the touching spheres, taking into account the various interaction energies, are collected in the Appendix. This appendix also describes how the subsequent neutron evaporation is taken into account. Neutron evaporation removes part of the spin of the nuclei prior to the γ cascading and should not be neglected. To investigate how assumptions about the geometry and the associated temperature influence the statistical spin distribution, we have performed calculations with both the

simplified Viola geometry and with touching spheres.

Another consideration is the correlation between the total angular momentum J and the mass partition. One extreme is to assign to all mass partitions one common average value of J, representing the mean angular momentum derived from the cross section for the quasifission-plus-fission reaction. Alternatively, one may assume that the largest mass drifts are achieved for the more central collisions, although it would be unrealistic to insist on symmetric mass divisions having a total angular momentum that is exactly zero. As a presumably realistic compromise, the quasifission cross section was divided in Ref. 9 into three equal bins, each bin being characterized by an average mass division and an average angular momentum $\langle J \rangle$. Each bin is also characterized by an average turning angle. This binning of the cross section is used to determine the relaxation time for the mass drift.[9] We here interpolate between these bin averages, obtaining smooth curves of $\langle J \rangle$ versus mass for each reaction. We use this running average for one set of statistical-model calculations, while the other set assumes a constant average. For symmetric mass splits the assigned values of the total angular momentum differ by about a factor of 2 in the alternative models. The reaction of 7.5 MeV/nucleon $^{238}U+^{48}Ca$ displays a nice direct mass versus angle differential cross section,[21,9] and we pick this reaction as an illustrative example.

The four panels of Fig. 9 display the calculated magnitude of the average spin in the two nuclei, as a function of mass partition, for two shapes and two assumptions about angular momentum fractionation. The aligned spin $\langle (S_A)_y \rangle$ and the spin dispersions in each nucleus combine in a nontrivial way to form the average spin magnitude $\langle S_A \rangle$. Comparing the two lowest curves within each panel, it is seen that the spin distribution is dominated by the dispersions at the elongated Viola shape. For touching spheres, dispersions and aligned spins contribute about equally. The larger spin variances found for the Viola shape result from the increase in temperature during the descent from the more compact shapes towards scission. The smaller aligned spin at the elongated Viola shape results from the larger total moment of inertia, and thereby the slower angular frequency. (The relative importance of aligned spins and dispersions is also illustrated in Fig. 11, but only for touching spheres.)

The thick curves in Fig. 9 display the quantity which is measured in the experiment, namely the sum of average spin magnitudes residing in the reaction products after neutron evaporation. These curves are quite flat, or mildly u shaped. This undramatic appearance as a function of mass partition actually results from the addition of two dramatically changing individual spins.

Except at very large mass asymmetry, the four different calculations shown in Fig. 9 mutually agree to better than 20 percent. Therefore, the figure shows that the overall magnitude of the spin predicted by the statistical equilibrium distribution is quite well defined, being relatively insensitive to details of the assumed shape or angular momentum fractionation.

Figure 10 compares these four different calculations to γ-ray multiplicity data for the ^{48}Ca target, both for 7.5 MeV/nucleon and for the smaller bombarding energy 5.9 MeV/nucleon. The standard relation $M_\gamma = S/2+6$ has been applied to calculate the gamma multiplicity from the angular momentum after neutron emission. This figure shows that the overall magnitude of the experimental spins is reproduced by the statistical equilibrium calculation for these two reactions, within typically 20 percent. This is the first major result. On the other hand, one sees from the figure that the experiments display a significantly stronger increase in the γ multiplicity with bombarding energy than predicted by the calculation. Furthermore, there is a problem of u shaped predictions and n-shaped measurements. We shall return to these problems in Secs. IV F and IV G.

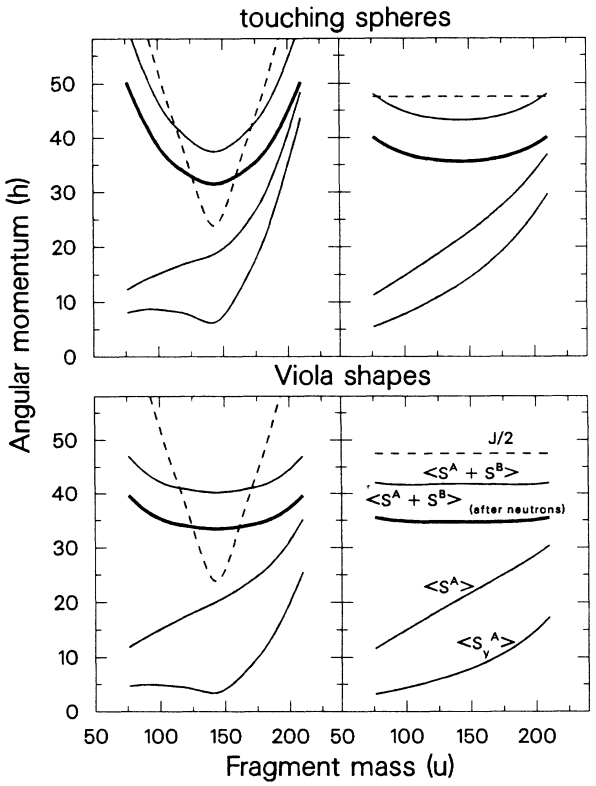

FIG. 9. Statistical-model calculation of the equilibrium spins carried by the reaction products for the reaction of 7.5 MeV/nucleon $^{238}U+^{48}Ca$. The two top panels are calculated with the geometry of touching spheres, and the two bottom panels refer to the schematic Viola shape. The left-hand panels assume angular momentum fractionation as described in the text, whereas a single average value is used for all masses in the right-hand side. The input angular momentum J is denoted by a dashed line. (For convenience of scale, one half of this quantity is shown.) Thin lines denote the average aligned spin $\langle S_y^A \rangle$ of one nucleus, the spin magnitude $\langle S_A \rangle$, and the sum of spin magnitudes $\langle S_A \rangle + \langle S_B \rangle$. Finally, the thick curve gives the quantity that is of experimental interest here, the sum of spin magnitudes in the two nuclei after neutron evaporation.

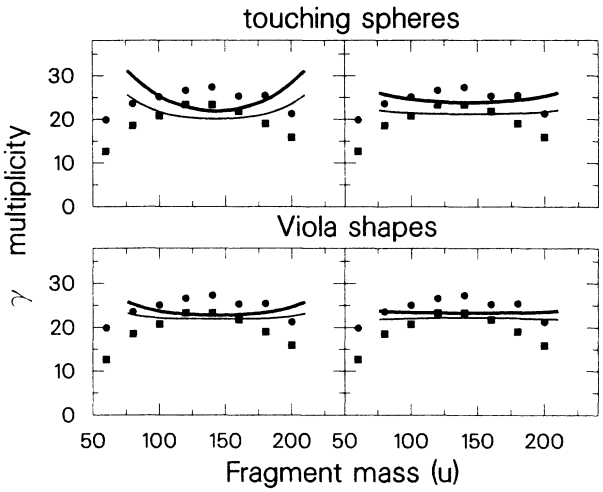

FIG. 10. Average γ-ray multiplicity M_γ for the $^{238}U+^{48}Ca$ reaction, related to the sum of spin magnitudes in the two nuclei after evaporation by the schematic equation $(\langle S_A+S_B\rangle)_{\text{after neutrons}}=2\times(M_\gamma-6)$. Data for 7.5 MeV/nucleon are denoted by dots and for 5.9 MeV/nucleon by squares. The calculated thick curve for 7.5 MeV/nucleon in the four panels is the same as shown in Fig. 9, and the lower curve in each panel presents the calculation for 5.9 MeV/nucleon.

C. Statistical-model results for a light target nucleus

Figure 11 shows a comparison for the two reactions 7.5 and 5.9 MeV/nucleon U+O. Again the different calculations agree to within better than 20 percent. The schematic Viola shape yields the largest spins due to the higher temperature, which is the dominating factor when the aligned spin is small.

D. The relative importance of spin fluctuations and mean spins

Figure 12 illustrates the relative importance of aligned spins and spin fluctuations as calculated for two different target nuclei. Thin curves display hypothetical γ multiplicities arising from the aligned spins alone, and, correspondingly, thick curves result from considering only dispersions. For the mean spin calculations, the last term of Eq. (11) has been ignored. The figure illustrates the dominance of fluctuations over mean spins, and shows that the fluctuations alone are in fact reasonably successful in explaining the overall magnitude of the observed γ-ray multiplicity in a broad mass range near symmetry.

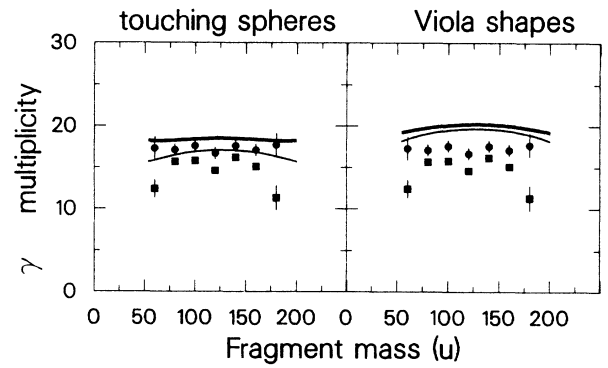

FIG. 11. Same as Fig. 10, for reactions with ^{16}O as a target nucleus. Since angular momentum fractionation is highly unlikely for these reactions, only calculations with constant average angular momentum vector as function of mass asymmetry are shown.

E. Overall result of the statistical model

Figures 13 and 14 show the result of the statistical-model calculation for all reactions. We have chosen what we consider the most realistic set of calculations, namely those where the geometry of touching spheres and angular momentum fractionation has been assumed. (Except for U+O, where a constant average spin is used.) The figure demonstrates the overall success of the statistical equilibrium model in explaining the spin magnitude near mass symmetry.

As already mentioned, two failures of the statistical equilibrium model in accounting for the data are apparent: (i) The calculated curves are flat, or mildly u shaped, whereas the data follow n-shaped curves. (ii) The calculation underpredicts the γ multiplicity at mass symmetry for the heaviest targets at the highest bombarding energies. In the following we will explore some possible origins of these two discrepancies.

F. Relaxation of spin versus mass

The occurrence of the n-shaped curves in the data (in contrast to the calculated u shaped or flat curves) may be

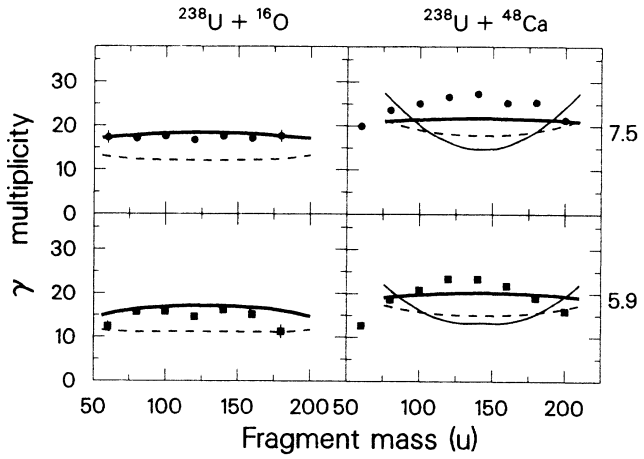

FIG. 12. Average γ-ray multiplicity calculated on the basis of either mean spins or variances alone, shown in comparison to data for 7.5 MeV and 5.9 MeV/arbitrary unit $^{238}U+^{16}O$ and $^{238}U+^{48}Ca$. Thick curves show the result calculated with variances alone, thin lines with mean spins alone, full drawn for angular momentum fractionation, and dashed lines with constant angular momentum. The shape consisting of touching spheres has been assumed.

an indication that some of the spin modes are not fully relaxed, that is, they never achieve full thermal excitation. As discussed in the Introduction, this is already known to happen for the tilting mode.[12]

The n-shaped curves can be understood through the following schematic consideration. Suppose that one has in a system two macroscopic variables, S (spin) and M (mass), which both relax in a diffusion process, S from its

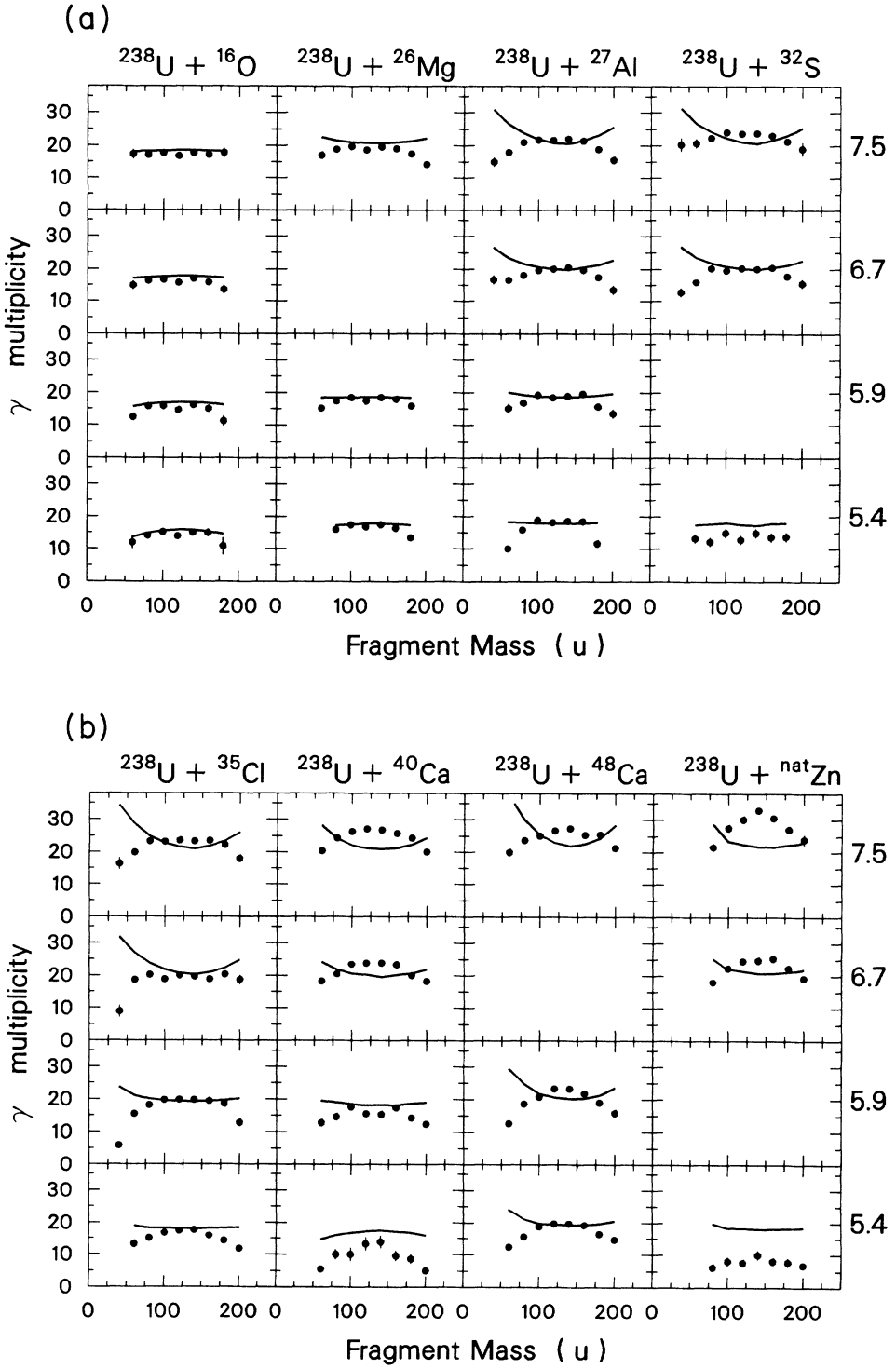

FIG. 13. (a) Overall comparison between calculated and mean γ-ray multiplicities for the lighter targets. The calculations are performed with the geometry of touching spheres, and also with angular momentum fractionation for targets heavier than oxygen. (b) Same as (a), but now for the heavier targets.

initial value 0 towards the value S_{eq}, and M from its initial value M_0 towards the value M_{eq}, with relaxation times τ_S and τ_M, respectively:

$$S = S_{eq}\left[1-\exp\left[-\frac{t}{\tau_S}\right]\right],$$
$$M = M_{eq}+(M_0-M_{eq})\exp\left[-\frac{t}{\tau_M}\right]. \quad (17)$$

The time, determined from the second equation, can be inserted into the first equation

$$S = S_{eq}\left[1-\left[\frac{|M_{eq}-M|}{|M_{eq}-M_0|}\right]^{\tau_M/\tau_S}\right], \quad (18)$$

which gives S as a power law function of M.

Figure 14 shows examples of such curves of two variables. The n-shaped curves obtained experimentally are seen to indicate that the spin distribution relaxes faster than the mass distribution, the ratio between relaxation times being of the order of $\tau_S \sim \frac{1}{3}\tau_M$.

Equation (18) can be used independently for each of the spin variances (10) and for the aligned spins (11) as well. They can subsequently be combined to form the total spin distribution. This gives many parameters, and it

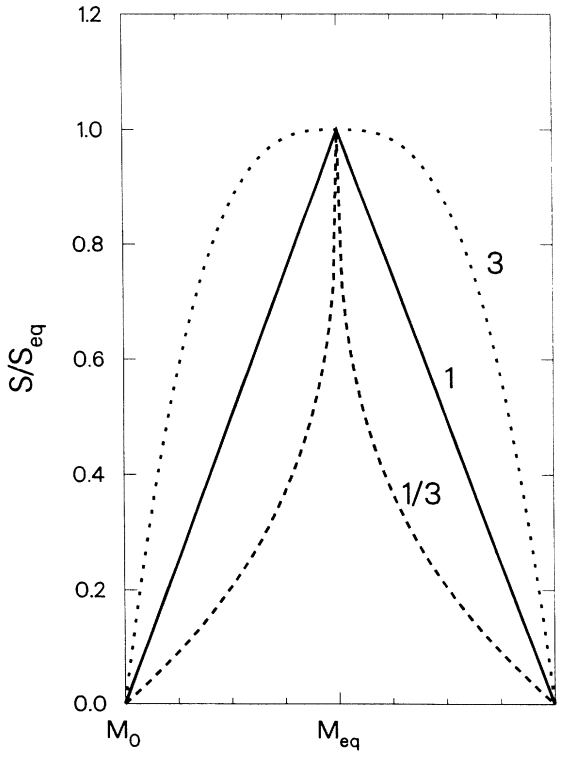

FIG. 14. Schematic relaxation curves for two quantities M (mass) and S (spin) that relax in the same reaction with two different relaxation times τ_M and τ_S. The curves are labeled with the ratio τ_M/τ_S.

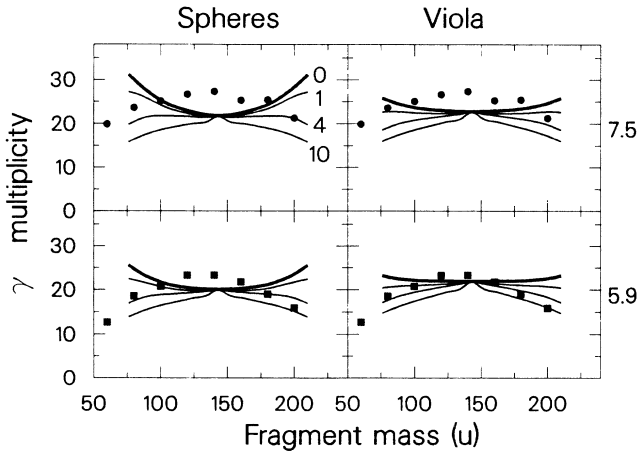

FIG. 15. Calculated average γ-ray multiplicities for the reactions of 7.5 MeV and 5.9 MeV/nucleon $^{238}U+^{48}Ca$, taking into account relaxation of the spin modes in the schematic way explained in the text. Thick curves show the statistical equilibrium distribution, and the lower curves, from above and down display the results obtained with the relaxation times obtained for window dissipation, four times these, and finally ten times these for the lowest curve.

makes no sense to vary them all freely. Instead we apply a set of typical relaxation times for window friction[7] in a comparison with the data. Figure 15 shows the results of this calculation, for both the compact and the Viola shape. Compared to a value of $\tau_M \simeq 5\times10^{21}$ s,[8,9] the typical spin relaxation times are as follows (Ref. 7): wriggling $\tau_S/\tau_M \simeq 0.05$, negative mode (bending and twisting) $\tau_S/\tau_M \simeq 0.2$, tilting $\tau_S/\tau_M \simeq 2$, and, correspondingly, for the mean values,[7] sliding $\tau_S/\tau_M \simeq 0.1$, rolling $\tau_S/\tau_M \simeq 0.4$. Since the spin magnitude is approximately given by the square root of the sum of the variances of the modes, the curve of the spin magnitude distribution tends to be dominated by the fastest relaxation time, which is very short. It is then not surprising that to reproduce the experimental n-shaped curves one needs longer relaxation times. Curves for four and ten times larger spin relaxation times are also shown in Fig. 15. In these calculations, the tilting relaxation time is kept, while all the others are scaled. This is because the tilting relaxation time $\tau_S/\tau_M \simeq 2$ is in reasonable accordance with angular distributions measured close to the beam axis.[12]

It is seen that the best calculated curves, as compared to experiment, are obtained with spin relaxation times about ten times larger than those calculated for window dissipation. With this choice of the scaling factor, the wriggling relaxation time becomes $\tau_S = \frac{1}{2}\tau_M$, and the remaining spin relaxation times are about $\tau_S \simeq 2\tau_M$. In this case, the spin distribution away from symmetry is dominated by the wriggling modes. This is in rough agreement with the discussion given above, since a u-shaped function S_{eq} in Fig. 14 would require a spin relaxation time of about $\tau_S \simeq \frac{1}{2}\tau_M$ to produce an n-shaped curve of the type seen experimentally. (The long relaxa-

tion times of the slow modes cause the S versus M curves in Fig. 15 to develop a spike of the type also shown in Fig. 14. This is artificial, since mass dispersions for a given impact parameter will round off such a spike.)

Incomplete spin relaxation taken into account in this way provides a very plausible explanation of the first of the above-mentioned failures of the equilibrium calculation, namely the inability to reproduce the n-shaped curves seen experimentally. Still, the calculations predict spin magnitudes which are too low at mass symmetry for the heavier target nuclei.

G. Compact geometry

To discuss the behavior of the spin magnitude at mass symmetry, we adopt again the parameter $T^{1/2}A^{5/6}$, which gives a quite good universal representation of the data, as shown in Fig. 7(c). The γ multiplicities at mass symmetry calculated for a touching spheres configuration (dashed curves) are compared to the data (open circles) for uranium-induced reactions in Fig. 16. The temperature used to compute the ordinate $T^{1/2}A^{5/6}$ is appropriate for the touching spheres configuration. The comparison illustrates once more the discrepancy between experimental data and model calculations, especially with regard to the slopes.

As a start, it may be of interest to compare these results to the prediction of a simple estimate, in which the aligned spin and the effects of neutron evaporation are neglected. In this case, we find the proportionality factor between the spin magnitude and $T^{1/2}A^{5/6}$ for the statistical spin distribution

$$\langle S_A + S_B \rangle \approx 2[\langle (S_A)^2 \rangle]^{1/2} \approx 2\sqrt{\tfrac{5}{7}+\tfrac{3}{2}}\sqrt{\mathcal{I}_A T} = 0.205 T^{1/2}A^{5/6} ,$$

or

$$\langle S_A + S_B \rangle = 2\sqrt{\tfrac{5}{7}+\tfrac{7}{10}+\tfrac{3}{2}}\sqrt{\mathcal{I}_A T} = 0.235 T^{1/2}A^{5/6} , \quad (19)$$

where tilting is excluded and included in the first and second estimates, respectively, and a mean square radius of $1.25A^{1/3}$ fm for the nuclei has been inserted.

These two estimates, after conversion to γ multiplicity, are shown as thin lines in Fig. 16 for the ^{nat}Zn target only. The more detailed calculations (thick-dashed curves) differ from these in two respects: the inclusion of aligned spin, and of neutron evaporation. Neutron evaporation is the most important, and the calculated curves actually displays a less steep slope. In general, the data

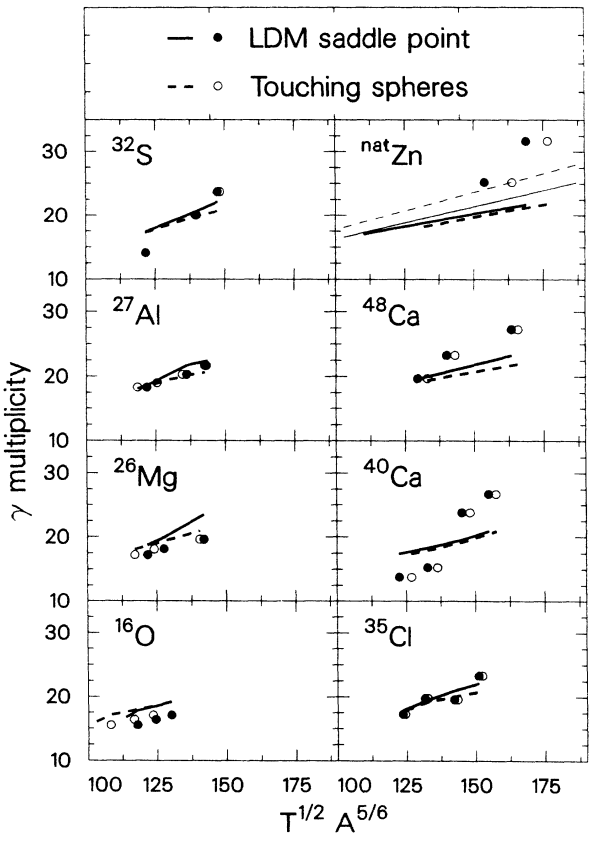

FIG. 16. Calculated and measured γ-ray multiplicities at mass symmetry, plotted as a function of the parameter $T^{1/2}A^{5/6}$. Open circles and dashed curves represent measured γ multiplicities and calculations for a touching spheres freeze-out configuration, whereas the filled circles and solid curves are associated with the increasingly compact shapes for the LDM saddle point.

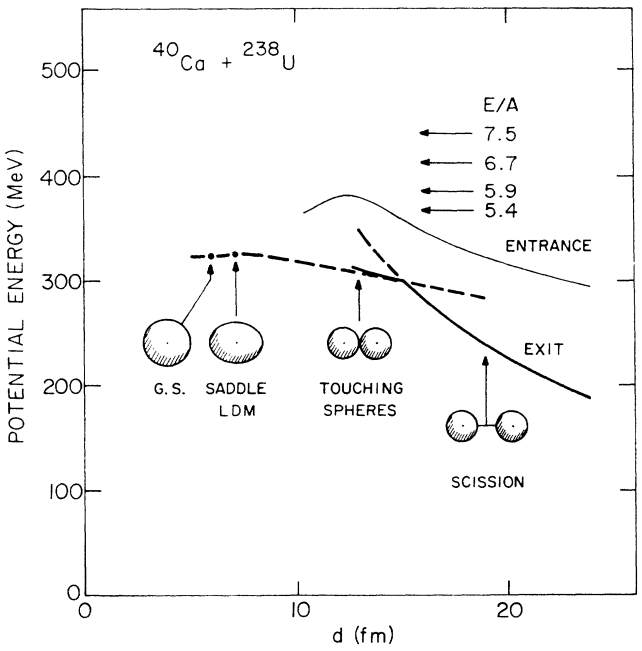

FIG. 17. Schematic potential energy as a function of distance between the two reaction products. The full drawn part of the curves are used in the calculations, and represent a schematic account of the neck formation. Dashed curves denote the continuation inward for the pure Coulomb repulsion assuming point charges, and outward for a shape with a considerable neck, respectively.

are sloping more steeply in Fig. 16 than any of the calculations shown. As one hypothesis that may explain this deviation, one may consider a change in compactness with total mass, and this we explore next in a rather schematic calculation. Most likely, the dinuclear complex spends most of its time at rather compact shapes (see Fig. 17). A representative compact shape may be the saddle shape of the composite system.

A very compact shape implies a very large effective moment of inertia for the tilting mode. The increase in tilting variance with increasing saddle shape compactness was actually proposed in Ref. 20 as an explanation of the γ-multiplicity data for the Pb-induced reactions. However, the more recent data on the tilting excitation by Lützenkirchen *et al.*[12] clearly rule out this explanation. But the other variances are affected by geometry as well. For a prolate ellipsoid, with major and minor axes $R_{\min}$, $R_{\max}$, chopped into two equally sized halves, one obtains for the orbital moment of inertia, and the sum of perpendicular moments of inertia of the two nuclei

$$\frac{\mathcal{I}_R}{\mathcal{I}_0}=\frac{45}{128}\left[\frac{R_{\max}}{R_0}\right]^2,$$
$$\frac{\mathcal{I}_{+,\perp}}{\mathcal{I}_0}=\frac{\mathcal{I}_{\text{tot},\perp}-\mathcal{I}_R}{\mathcal{I}_0}=\frac{19}{128}\left[\frac{R_{\max}}{R_0}\right]^2+\frac{1}{2}\left[\frac{R_{\min}}{R_0}\right]^2, \tag{20}$$

in units of the moment of inertia of the spherical compound nucleus $\mathcal{I}_0$ and its radius R_0. These moments of inertia are relevant for the wriggling variances, and the momenta of inertia of the other modes follow likewise from simple geometrical considerations.

The thick solid curves in Fig. 16 represents the γ multiplicity calculated on the basis of the statistical model with these expressions for the moments of inertia. The values of $R_{\min}$ and $R_{\max}$ are chosen in accordance with the nonrotating liquid-drop model predictions of the saddle shapes. An exception is the contribution from tilting, which is deduced from experiment,[12] corresponding to half the statistical excitation at touching spheres. The results (thick solid curves) of such a schematic calculation are compared to the data in Fig. 16 (solid circles). Note that the nuclear temperature associated with this configuration is different from the temperature for touching spheres. Using the generally more compact and also variable saddle shape of the assumed freeze-out configuration improves the agreement with data somewhat, without in any way giving a satisfactory fit to the data. The larger moments of inertia associated with the negative modes are responsible for both the increase in the average spin magnitude and for the increase in slope. The wriggling moments of inertia, on the other hand, decrease with increasing compactness. Some of the remaining discrepancy could actually be removed by letting the wriggling modes adjust to the elongation of the shape in the later phases of the reaction. With the crude models available at present, we shall not attempt to quantify this possibility. We therefore conclude the present schematic comparison by observing that in addition to the incomplete relaxation processes, changes in the geometry of the assumed freeze-out configuration seem to play a role in these reactions. The changes are in the same direction but stronger than the changes in the liquid-drop saddle shape. One may speculate that the relevant shapes will become increasingly compact, even for a fixed projectile-target combination, when the bombarding energy and, hence, the excess radial energy increases. Such an effect would make the calculated curves (thick lines in Fig. 16) steeper. At any rate, the implication is that the freeze out of the thermal spins occurs at a surprising early stage, where the shapes are still quite compact (and the motion slow). The observed tendency towards rather long spin-relaxation times adds plausibility to this conjecture.

V. SUMMARY AND CONCLUSION

The γ multiplicities measured in this present work are shown as a function of fragment mass in Figs. 5 and 6. We observe that the γ-multiplicity curves change from being slightly u shaped for the ^{16}O target to becoming increasingly n shaped for heavier targets, the highest γ multiplicities being found for mass symmetric mass divisions. As illustrated in Fig. 7, we find that the γ multiplicity for symmetric mass splits shows the trend expected for purely thermal excitations of the fragment spin modes, namely an increasing γ multiplicity with a reasonably tight correlation with the parameter $T_{\text{CN}}^{1/2}A_{\text{CN}}^{5/6}$. The dependence on this parameter is, however, steeper than expected, which may indicate a more complicated dependence on, e.g., the total spin **J** and the freeze-out shape.

The experimental results on the spin magnitude for fragments from fission and quasifission reactions are interpreted in more detail by comparison with a statistical "equilibrium" model.

First, the model prediction of the spin magnitude has been investigated in itself, with regard to its dependence upon the geometry and on the functional form of the total angular momentum versus fragment mass. A certain dependence on both was found, especially at large mass asymmetry.

For the reaction with the lightest target, which is of the compound fission type, the statistical equilibrium model gives a very precise description of the data. However, for heavier targets, and for the largest bombarding energy, where quasifission dominates, specific deviations between the statistical equilibrium model calculations and data are found.

In order to understand the deviations, the statistical-model calculations have been modified to take into account the finite relaxation times of the spin modes, and the varying compactness of the freeze-out shape. The n-shaped experimental curves of spin versus mass can be roughly understood, if the spin mode relaxation times are assumed to be about $\frac{1}{3}$ to $\frac{1}{2}$ of the mass relaxation time 5×10^{-21} s, or about four to ten times longer than those calculated for window dissipation, applicable to deep-inelastic reactions. Such relaxation times are surprisingly long. Furthermore, the steeply increasing M_γ values

found at high excitation energy for the heavier systems may be related to variations in the compactness of the reaction complex at freeze out. This is here qualitatively calculated by applying the saddle-shape geometry for all modes except tilting, which is kept at a value in accordance with measurements.[12] This modification of the model brings the predicted multiplicities closer to the experimental values.

Thus, this study indicates that quantitative studies of the angular momentum relaxation in quasifission reactions carry important information both on the time-dependent relaxation of the spin degrees of freedom and on the freeze-out geometry. The study serves, chiefly, to emphasize the importance of thermally generated fragment spins, compared to the role of aligned angular momentum. In these reactions M_γ is a very poor measure of the reaction angular momentum. In addition, one finds time constants for thermal spin relaxation that are distinctly longer than found in deep-inelastic reaction studies. This is to be contrasted to the mass asymmetry relaxation, where the corresponding time is distinctly shorter. A theoretical understanding of this is still lacking. Finally, the systematic trends in the measurements, when plotted versus $T^{1/2}A^{5/6}$, leads to conjectured freeze-out shapes for thermal spin relaxation that are surprisingly compact. They tend to vary in the same way the saddle shapes do, though even more strongly. The theoretical understanding of this observation is incomplete.

Basically, we understand deep-inelastic reactions with reasonable success in terms of dinuclear one-body dissipation, and quasifission reactions as cases of mononucleus (i.e., wall) dissipation; but how the transition between the two regimes is to be understood remains a major challenge.

ACKNOWLEDGMENTS

This work was supported by the U.S. Department of Energy, Nuclear Physics Division, under Contract W-31-109-Eng-38. One of us (B.B.B.) wishes to acknowledge financial support from the Danish Natural Science Foundation.

APPENDIX

This appendix describes how the temperature at the various geometries is estimated, as well as the expressions used for taking into account the neutron evaporation. Since the nuclei in question are heated and rotating, only the liquid-drop part of their total binding energy should be taken into account. The thermal energy in the final nuclei, given by the Viola systematics, is then

$$E^* = E_{\text{c.m.}} + Q - E_{\text{rot}} - V \ . \tag{21}$$

Here $E_{\text{c.m.}}$ is the center of mass in the entrance channel and Q is the Q value of the reaction obtained by using experimental entrance channel masses and liquid-drop model estimates of the exit channel masses. E_{rot} denotes the mean rotation energy, which is calculated with the mean spins according to the actual spin distribution, either the statistical equilibrium values, or with inclusion of finite relaxation times. V is the Coulomb energy of two nuclei at the scission point

$$V = \frac{e^2 Z_1 Z_2}{r_s (A_1^{1/3} + A_2^{1/3})} \ , \tag{22}$$

where $r_s = 1.83$ fm is the experimentally obtained distance parameter.[28]

The more compact shapes are cooler because of their larger Coulomb energy, which, on the other hand, is compensated to some extent by the reduction in the surface energy due to neck formation. Our estimate of the influence of neck formation is inferred from the potential surfaces compiled by Blocki and Swiatecki[29] for the fissilities in question. These display roughly the following behavior: When the distance is decreased from the Viola distance, the minimal energy for a given distance is found for neck radius 0 until the two nuclei come in at a distance of approximately $1.47(A_1^{1/3} + A_2^{1/3})$ fm. For smaller distances, the potential energy is lowered if a neck can be formed. Viewed as a function of the distance, the potential energy curve is much flatter with a neck than with the pure Coulomb potential. For a neck radius of about half of the average radius of the nuclei, neck formation will reduce the steepness of the potential energy curve by about a factor of 4, as illustrated in Fig. 17. This leads us to the following schematic parametrization of the potential with neck, which we use to estimate the thermal energy at the touching spheres configuration:

$$V \approx \frac{e^2 Z_1 Z_2}{A_1^{1/3} + A_2^{1/3}} \left[\frac{0.25}{r} + \frac{0.75}{1.47} \right] . \tag{23}$$

For touching spheres, the radius parameter $r = 1.25$ is inserted. Finally, the temperature at either shape is calculated according to the usual expression

$$T = \left[\frac{E^*}{a} \right]^{1/2} , \tag{24}$$

where the level density constant is chosen in a standard way as $a = (A_1 + A_2)/10$ MeV^{-1}. The amount of angular momentum removed by the neutron evaporation cannot be ignored, as illustrated in Fig. 9.

To estimate the neutron evaporation, we first divide the thermal energy, Eq. (21), in the two final nuclei in proportion to their mass. The average angular momentum in one of the nuclei after neutron evaporation is related to the spin S_0 prior to the evaporation approximately as [Ref. 30, Eq. (A24)]

$$\langle S \rangle_{\text{after neutrons}} = S_0 \exp \left[-\langle n \rangle \left[\frac{2}{3} \frac{mR^2}{\mathcal{J}} + \frac{\hbar^2}{2\mathcal{J}T_1} - \frac{4}{9} \frac{mR^2 T_1}{S_0^2} \right] \right] . \tag{25}$$

Here the number of emitted neutrons is denoted by $\langle n \rangle$,

m is the neutron mass, and T_1, R, and $\mathcal{J}$ are the temperature, radius, and rigid moment of inertia of the first daughter nucleus, respectively. The parameters used in Eq. (25) are given in Eq. (A27) of Ref. 30. Here we wish only to point to the rather large effective barrier radius $1.95A^{1/3}$ fm for the neutron evaporation, considerably larger than expected on the basis of a naive geometrical consideration.

*Present address: Institute of Modern Physics, Lanzhou, People's Republic of China.

[1]C. F. Tsang, Phys. Scr. **10A**, 90 (1974).
[2]R. Albrecht, W. Dünnweber, G. Graw, H. Ho, S. G. Steadman, and J. P. Wurm, Phys. Rev. Lett. **34**, 1400 (1975).
[3]P. Dyer, R. J. Puigh, R. Vandenbosch, T. D. Thomas, M. S. Zisman, and L. Nunnelly, Nucl. Phys. **A322**, 205 (1979).
[4]D. von Harrach, P. Glässel, Y. Civelekoglu, R. Männer, and H. J. Specht, Phys. Rev. Lett. **42**, 1728 (1979).
[5]S. Ayik, G. Wolschin, and W. Nörenberg, Z. Phys. **286**, 271 (1976).
[6]L. Moretto and R. P. Schmitt, Phys. Rev. C **21**, 204 (1980).
[7]T. Døssing and J. Randrup, Nucl. Phys. **A433**, 215 (1985).
[8]W. Q. Shen *et al.*, Europhys. Lett. **1**, 113 (1987).
[9]W. Q. Shen, J. Albinski, A. Gobbi, S. Gralla, K. D. Hildenbrand, N. Herrmann, J. Kuzminski, W. F. J. Müller, H. Stelzer, J. Tōke, B. B. Back, S. Bjørnholm, and S. P. Sørensen, Phys. Rev. C **36**, 115 (1987).
[10]C. Gerschel, M. A. Delaplanque, M. Ishihara, C. Ngô, N. Perrin, J. Péter, B. Tamain, L. Valentin, D. Paya, Y. Sugiyama, M. Berlanger, and F. Hanappe, Nucl. Phys. **A317**, 473 (1979).
[11]J. Blocki, H. Feldmeier, and W. J. Swiatecki, Nucl. Phys. **A459**, 145 (1986).
[12]K. Lützenkirchen, J. V. Kratz, G. Wirth, W. Brüchle, K. Sümmerer, R. Lucas, J. Poitou, and C. Gregoire, Nucl. Phys. **A452**, 351 (1986).
[13]R. F. Reising, G. L. Bate, and J. R. Huizenga, Phys. Rev. **141**, 1161 (1966).
[14]B. B. Back, R. R. Betts, K. Cassidy, B. G. Glagola, J. E. Gindler, L. E. Glendenin, and B. D. Wilkins, Phys. Rev. Lett. **50**, 818 (1983).
[15]B. B. Back, R. B. Betts, J. E. Gindler, B. D. Wilkins, S. Saini, M. B. Tsang, C. K. Gelbke, W. G. Lynch, M. A. McMahan, and P. A. Baisden, Phys. Rev. C **32**, 195 (1985); **33**, 385 (1986).
[16]B. B. Back, Phys. Rev. C **31**, 2104 (1985); **32**, 1786 (1985).
[17]T. Døssing and J. Randrup, Phys. Lett. **155B**, 333 (1985).
[18]R. Schmitt, G. Mouchaty, D. R. Haenni, and P. Bogucki, Phys. Lett. **127B**, 327 (1983).
[19]F. A. Dilmanian, L. Grozins, J. W. Ball, M. Beckerman, R. Boisseau, S. Gazes, R. Ledoux, and A. Sperduto, Phys. Lett. **127B**, 172 (1983).
[20]R. Bock, Y. T. Chu, M. Dakowski, A. Gobbi, E. Grosse, A. Olmi, H. Sann, D. Schwalm, U. Lynen, W. Müller, S. Bjørnholm, E. Esbensen, W. Wölfi, and E. Morenzoni, Nucl. Phys. **A388**, 334 (1982).
[21]J. Tōke, R. Bock, G. X. Dai, A. Gobbi, S. Gralla, K. D. Hildenbrand, J. Kuzminski, W. F. J. Müller, A. Olmi, H. Stelzer, B. B. Back, and S. Bjørnholm, Nucl. Phys. **A440**, 327 (1985).
[22]A. J. Sierk, Phys. Rev. C **33**, 2039 (1986).
[23]P. Glässel, R. S. Simon, R. M. Diamond, R. C. Jarad, I. Y. Lee, L. G. Moretto, J. O. Newton, R. Schmitt, and F. S. Stephens, Phys. Rev. Lett. **38**, 331 (1977).
[24]J. B. Wilhelmy, E. Cheifetz, R. C. Jared, S. G. Thompson, H. R. Bowman, and J. O. Rasmussen, Phys. Rev. C **5**, 2041 (1972).
[25]J. Randrup, Nucl. Phys. **A307**, 319 (1978).
[26]J. R. Nix and W. J. Swiatecki, Nucl. Phys. **71**, 1 (1965).
[27]R. P. Schmitt and A. J. Pacheco, Nucl. Phys. **A379**, 313 (1982).
[28]V. E. Viola, Phys. Rev. C **31**, 1550 (1985).
[29]J. Blocki and W. J. Swiatecki, Lawrence Berkeley Laboratory Report No. LBL-12811, 1982.
[30]T. Døssing and J. Randrup, Nucl. Phys. **A433**, 280 (1985).

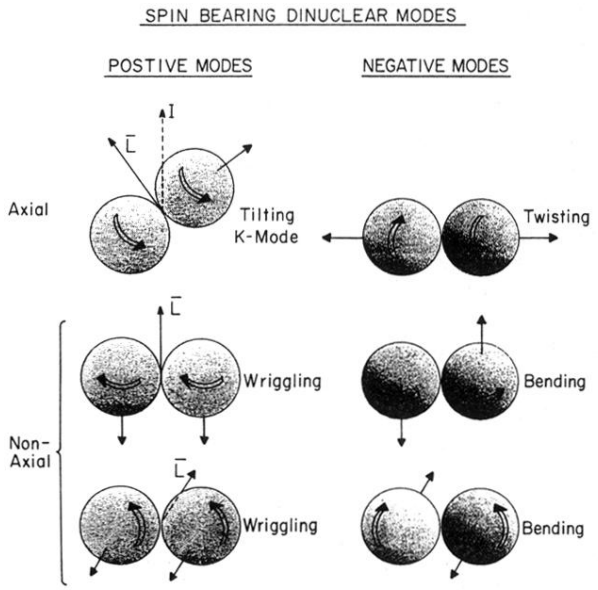

FIG. 1. Schematic illustration of the six statistical spin modes of a dinuclear system based on Ref. 6.

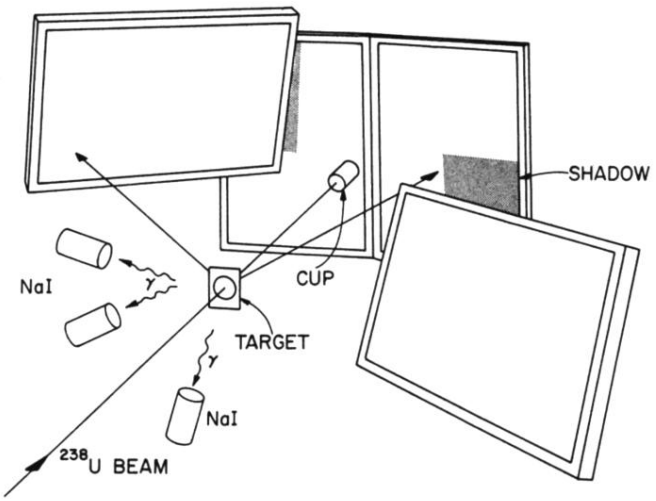

FIG. 2. Schematic illustration of the experimental arrangement used in this work.

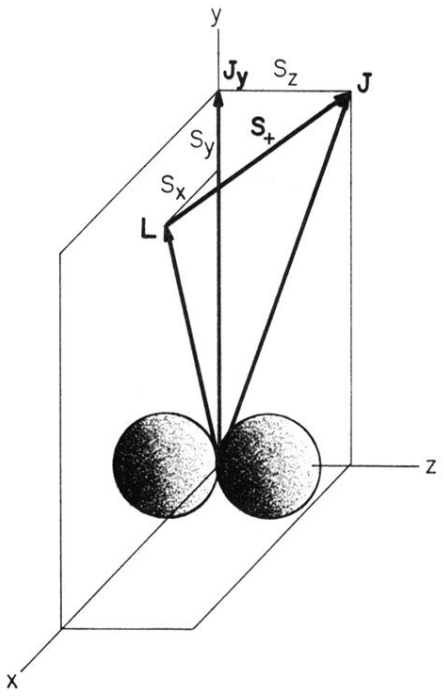

FIG. 8. Schematic illustration of the $\mathbf{J}_y$-aligned coordinate system used in this work.